Guo et al. *Zool. Res.* 2023, 44(3): 451−466
https://doi.org/10.24272/j.issn.2095-8137.2023.031

ZR | Zoological Research

Article Open Access

Cell atlas of CCl_4-induced progressive liver fibrosis reveals stage-specific responses

Peng-Cheng Guo[1,2,3,#], Jing Zuo[2,3,#], Ke-Ke Huang[4], Guang-Yao Lai[2,3,5,6], Xiao Zhang[1,2,3], Juan An[2,3,5,7], Jin-Xiu Li[2,3,8], Li Li[5], Liang Wu[5], Yi-Ting Lin[5], Dong-Ye Wang[5], Jiang-Shan Xu[2,3], Shi-Jie Hao[2,3,8], Yang Wang[2,3], Rong-Hai Li[2,3], Wen Ma[2,3], Yu-Mo Song[2,3], Chang Liu[2,3], Chuan-Yu Liu[2,3], Zhen Dai[9], Yan Xu[10], Amar Deep Sharma[11], Michael Ott[11], Qing Ou-Yang[12], Feng Huo[12], Rong Fan[13], Yong-Yin Li[13], Jin-Lin Hou[13], Giacomo Volpe[14], Long-Qi Liu[2,3], Miguel A. Esteban[1,2,3,4,5,6,15,*], Yi-Wei Lai[2,3,*]

[1] *State Key Laboratory for Zoonotic Diseases*, *Key Laboratory for Zoonosis Research of Ministry of Education*, *Institute of Zoonosis*, *College of Veterinary Medicine*, *Jilin University*, *Changchun*, *Jilin* 130062, *China*
[2] *BGI-Hangzhou*, *Hangzhou*, *Zhejiang* 310012, *China*
[3] *BGI-Shenzhen*, *Shenzhen*, *Guangdong* 518083, *China*
[4] *Key Laboratory of Biological Targeting Diagnosis*, *Therapy and Rehabilitation of Guangdong Higher Education Institutes*, *Fifth Affiliated Hospital of Guangzhou Medical University*, *Guangzhou*, *Guangdong* 510799, *China*
[5] *Laboratory of Integrative Biology*, *Guangzhou Institutes of Biomedicine and Health*, *Chinese Academy of Sciences*, *Guangzhou*, *Guangdong* 510530, *China*
[6] *Joint School of Life Sciences*, *Guangzhou Institutes of Biomedicine and Health and Guangzhou Medical University*, *Guangzhou*, *Guangdong* 510530, *China*
[7] *School of Life Sciences*, *Division of Life Sciences and Medicine*, *University of Science and Technology of China*, *Hefei*, *Anhui* 230026, *China*
[8] *College of Life Sciences*, *University of Chinese Academy of Sciences*, *Beijing* 100049, *China*
[9] *Guangzhou Institutes of Biomedicine and Health*, *Chinese Academy of Sciences*, *Guangzhou*, *Guangdong* 510530, *China*
[10] *Biotherapy Centre*, *Third Affiliated Hospital of Sun Yat-sen University*, *Guangzhou*, *Guangdong* 510630, *China*
[11] *Department of Gastroenterology*, *Hepatology and Endocrinology*, *Hannover Medical School*, *Hannover* 30625, *Germany*
[12] *Department of Hepatobiliary Surgery and Liver Transplant Center*, *General Hospital of Southern Theater Command*, *Guangzhou*, *Guangdong* 510010, *China*
[13] *Department of Infectious Diseases*, *Nanfang Hospital*, *Southern Medical University*, *Guangdong Provincial Key Laboratory of Viral Hepatitis Research*, *Guangzhou*, *Guangdong* 510515, *China*
[14] *Hematology and Cell Therapy Unit*, *IRCCS-Istituto Tumori 'Giovanni Paolo II'*, *Bari* 70124, *Italy*
[15] *Institute of Experimental Hematology*, *Hannover Medical School*, *Hannover* 30625, *Germany*

ABSTRACT

Chronic liver injury leads to progressive liver fibrosis and ultimately cirrhosis, a major cause of morbidity and mortality worldwide. However, there are currently no effective anti-fibrotic therapies available, especially for late-stage patients, which is partly attributed to the major knowledge gap regarding liver cell heterogeneity and cell-specific responses in different fibrosis stages. To reveal the multicellular networks regulating mammalian liver fibrosis from mild to severe phenotypes, we generated a single-nucleus transcriptomic atlas encompassing 49 919 nuclei corresponding to all main liver cell types at different stages of murine carbon tetrachloride (CCl_4)-induced progressive liver fibrosis. Integrative analysis distinguished the sequential responses to injury of hepatocytes, hepatic stellate cells and endothelial cells. Moreover, we reconstructed the cell-cell interactions and gene regulatory networks implicated in these processes. These integrative analyses uncovered previously overlooked aspects of hepatocyte proliferation exhaustion and disrupted

Received: 27 January 2023; Accepted: 11 March 2023; Online: 13 March 2023

Foundation items: This work was supported by the National Natural Science Foundation of China (32200688, 92068106, U20A2015, 32211530050), Guangdong Basic and Applied Basic Research Foundation (2021B1515120075, 2021A1515110180), and Science and Technology Program of Guangzhou (202201010408, 202201011037)

[#]Authors contributed equally to this work

*Corresponding authors, E-mail: miguelesteban@genomics.cn; laiyiwei@genomics.cn

pericentral metabolic functions, dysfunction for clearance by apoptosis of activated hepatic stellate cells, accumulation of pro-fibrotic signals, and the switch from an anti-angiogenic to a pro-angiogenic program during CCl_4-induced progressive liver fibrosis. Our dataset thus constitutes a useful resource for understanding the molecular basis of progressive liver fibrosis using a relevant animal model.

Keywords: Liver fibrosis; Toxicity; Single-cell and single-nucleus RNA-sequencing; Hepatocytes; Hepatic stellate cells; Angiogenesis; Cell-cell interactions; Gene regulatory networks

INTRODUCTION

The liver is a multifunctional organ only found in vertebrates (Shiojiri et al., 2018). Liver fibrosis is the frequent consequence of a sustained wound-healing response resulting from a wide variety of chronic liver injuries (e.g., viral hepatitis, alcoholism, and non-alcoholic steatohepatitis) (Sarin et al., 2020). These pathological conditions affect a large proportion of humans. Activation of hepatic stellate cells (HSCs), which then gain a myofibroblast-like phenotype, is a major driver of this process. This leads to aberrant synthesis and deposition of extracellular matrix (ECM) proteins, which ultimately generate fibrotic scars. Concomitantly, liver injury is often accompanied by various pathological responses, including robust inflammatory reactions, massive hepatocyte death with associated compensatory proliferation and metabolic shifts, and the capillarization of hepatic sinusoids, which progresses to pathological angiogenesis (Kisseleva & Brenner, 2021; Tsuchida & Friedman, 2017). Notably, these physiological changes and processes potentiate fibrosis progression.

Clinical and experimental studies have revealed that the degree of liver fibrosis substantially affects patient morbidity and mortality. Mild liver fibrosis can be reversed by apoptosis, senescence, or de-differentiation of activated HSCs (aHSCs) upon cessation of injury. However, progressive liver fibrosis during long-term injury has a high risk of developing into liver cirrhosis with chronically impaired liver function and a high incidence of hepatocellular carcinoma (Tsuchida & Friedman, 2017). Current therapies for late liver fibrosis and cirrhosis have limited efficacy (Ramachandran et al., 2019). Thus, developing novel approaches for reversing liver fibrosis at any stage is of utmost importance to meet clinical needs. To facilitate this, it is necessary to clarify how liver fibrosis progression is coordinated at the molecular level throughout different stages. Currently, this is not well understood, in part due to the heterogeneity of resident parenchymal and non-parenchymal liver cells and their distinct responses at different stages of chronic injury.

Recent advances in single-cell transcriptomic technologies have provided unprecedented insights into the heterogeneity and molecular dynamics of different cell types and states in the fibrotic/cirrhotic liver. These advancements have expanded our understanding of the scar-associated subpopulations in cirrhotic human liver (Ramachandran et al., 2019), provided insights into the HSC activation roadmap in early murine liver fibrosis induced by carbon tetrachloride (CCl_4) or bile duct ligation (Krenkel et al., 2019; Yang et al., 2021), characterized the association between hepatocyte death and HSC activation in CCl_4-induced murine liver fibrosis (Mederacke et al., 2022), clarified the role of HSCs in human and murine (CCl_4- and diethylnitrosamine-induced) hepatocarcinogenesis (Filliol et al., 2022), and determined key events driving liver sinusoidal endothelial cell (LSEC) capillarization in CCl_4-induced murine liver cirrhosis (Su et al., 2021). However, these studies are limited to specific stages of liver fibrosis and/or specific liver cell types, thereby hindering our understanding of the events underlying the overall process.

Given their many shared characteristics with the human liver, rodents, in particular mice, are widely used to study mammalian liver function. To obtain a molecular overview of the pathogenesis of progressive liver fibrosis, we applied single-nucleus RNA-sequencing (snRNA-seq) in a mouse model of CCl_4-induced liver fibrosis at different stages. Initial exposure of the mouse liver to CCl_4 induces necrosis in hepatocytes located around the central vein, which are responsible for most liver detoxification functions, closely mimicking aspects of human chronic hepatotoxicity. Importantly, continued treatment leads to progressive liver fibrosis. Here, we generated an atlas of progressive liver fibrosis encompassing transcriptomic information from 49 919 nuclei covering a variety of liver cell types. Using this map, we studied the kinetics of hepatocyte proliferation, zonal metabolic dysfunction, HSC activation, and LSEC capillarization/angiogenesis at different stages of chronic liver damage. To complement and/or validate aspects of our work, we also reanalyzed data from previously published studies (Filliol et al., 2022; Mederacke et al., 2022; Yang et al., 2021). In addition, we investigated the cell-cell communication networks and intrinsic gene regulatory networks (GRNs) coordinating stage-specific responses. Our study offers an integrative and dynamic view of progressive liver fibrosis, providing a rich resource for identifying potential therapeutic targets.

MATERIALS AND METHODS

Animal experiments

All animal experiments were performed in accordance with the regulations of the Animal Care and Use Committee of the Guangzhou Institutes of Biomedicine and Health under license No. IACUC2018038. Specific pathogen-free C57BL/6 mice were bred and housed in a temperature- and light-controlled (12 h-light/dark cycle) animal facility. Male mice at 6 weeks of age were used for all experiments. CCl_4-induced liver fibrosis was generated by administering 0.5 mL/kg of CCl_4 (Macklin, C822982, China) diluted in oil (1:4) via intraperitoneal injection twice a week. Control animals were treated with oil only at the same time intervals. Both control and experimental mice were sacrificed at selected time points. Whole livers were isolated, cut into small pieces, and snap frozen in liquid nitrogen for snRNA-seq library preparation or fixed in 4% paraformaldehyde (Biosharp, BL539A, China) for staining experiments.

Single-nucleus RNA-sequencing library construction

The frozen liver fragments were used for single-nucleus isolation performed via a mechanical separation protocol with a 2 mL Dounce apparatus (Sigma, D8938, USA), as described previously (Han et al., 2022; Ma et al., 2022). Isolated nuclei were diluted with 0.04% bovine serum albumin (BSA, Absin, abs49001013a, China) in phosphate-buffered saline (PBS) for library preparation using the DNBelab C Series Single-Cell

Library Prep Set (MGI, 1000021082, China) according to the manufacturer's instructions. Briefly, the nuclear suspension and barcoded beads were loaded on the chip for droplet encapsulation. Beads were collected for reverse transcription using the following parameters: 10 cycles at 50 °C for 2 min followed by a step at 42 °C for 2 min. The cDNA-containing beads were then collected for second-strand cDNA synthesis and amplified using the following parameters: 95 °C for 3 min; 16 cycles at 98 °C for 20 s, 60 °C for 30 s, and 72 °C for 3 min, followed by a step at 72 °C for 10 min. At this stage, cDNA and droplet barcode products were purified for standard barcoded sequencing library construction. Libraries were assessed using an Agilent Bioanalyzer and sequenced using a DIPSEQ T1 sequencer at the China National GeneBank (CNGB, Shenzhen) with the following read lengths: cDNA: 30 bp for read 1 and 100 bp for read 2; droplet barcode: 20 bp for read 1 and 30 bp for read 2.

Immunofluorescence, single-molecule fluorescence *in situ* hybridization (smFISH), and histological staining

Liver tissues were fixed overnight in 4% paraformaldehyde at 4 °C and embedded in paraffin blocks. Immunofluorescence, smFISH, and Masson staining experiments were performed on 5 μm thick paraffin-embedded sections. Paraffin sections were incubated in xylene (Macklin, X821391, China) three times (10 min each time) for deparaffinization, then rehydrated through serial incubation with decreasing concentrations of ethanol (100%, 90%, 80%, 70%, and 50%), with a final wash in ddH_2O. For immunofluorescence staining, sections were further processed using an improved citrate antigen retrieval solution (Beyotime, P0083, China). After this, they were blocked with 5% donkey serum (Jackson Immuno Research, 017-000-121, USA) and 5% goat serum (Beyotime, C0265, China), followed by staining with primary antibody against glutamine synthetase (GS, Abcam, ab49873, USA) at 1:500 dilution overnight at 4 °C and incubation with the corresponding fluorescent conjugated secondary antibody at 1:500 dilution for 1 h at room temperature. For smFISH, sections were stained using RNAscope Fluorescent Multiplex and RNAscope Multiplex Fluorescent v2 (Advanced Cell Diagnostics, 323100, USA) according to the manufacturer's instructions. The sections were then stained with 4',6-diamidino-2-phenylindole (DAPI, Sigma, D9542, USA) and images were taken with an Olympus IXplore SpinSR. For Masson staining, sections were sequentially stained with hematoxylin (Beyotime, C0107, China), Ponceau S (Beyotime, P0022, China), and aniline blue (Solarbio, A9540, China). Images were taken with a Zeiss Observer Z2 microscope and stained areas were evaluated by ImageJ (v1.53c) using a color deconvolution plugin.

Raw data processing

Raw sequencing reads were filtered, demultiplexed, and aligned to the mm10 reference genome using an in-house workflow (v2.0.7, https://github.com/MGI-tech-bioinformatics/DNBelab_C_Series_HT_scRNA-analysis-software). To increase sensitivity, we included the intron-containing reads for gene expression analysis. The resulting count matrices were filtered by unique molecular identifiers (UMIs) >2 000 (corresponding to a minimum number of 508 genes) and mitochondrial gene content <20%. Doublets were identified and filtered using DoubletFinder (v2.0.3). The ambient RNA contamination rate was estimated using SoupX (Young & Behjati, 2020) with default settings.

Clustering and cell annotation

Global clustering was performed using Scanpy (v1.8.2) (Wolf et al., 2018) in a Python (v3.7) environment. In brief, filtered data were normalized by the total count, followed by dimension reduction using principal component analysis (PCA) of the top 3 000 highly variable genes, in which the effects of UMIs and the percentage of mitochondrial genes were regressed out and scaled with default options. Batch effects between different libraries were corrected by Harmony (Korsunsky et al., 2019). The batch effect-corrected top 30 principal components were used for generating the neighborhood graph with the number of neighbors set to 10. Cell clustering was performed using the Louvain algorithm with resolution set to 0.8, and the resultant clusters were annotated using canonical markers. Published data were downloaded from the Gene Expression Omnibus with the following accession numbers: GSE171904 (Yang et al., 2021), GSE212047 (Filliol et al., 2022), and GSE172492 (Mederacke et al., 2022).

Differential gene expression and functional enrichment analysis

Scanpy was used to determine differentially expressed genes (DEGs) for each cell type between time points. The obtained DEGs for each comparison were used as input in Metascape (v3.5) (Zhou et al., 2019) with default settings.

Pseudotime analysis

For Monocle2 (v2.20.0) (Qiu et al., 2017) pseudotime analysis, the DEGs between HSCs in the CCl_4 and control groups at each time point were used for DDRTree analysis (*reduceDimension*) and pseudotime ordering (*orderCells*).

Psupertime analysis

For psupertime (v0.2.6) (Macnair et al., 2022) supervised pseudotime analysis, data were converted into *SingleCellExperiment* class and aligned along the temporal trajectory based on DEGs between the CCl_4 and control groups at each time point for each cell type. DEGs were clustered using the *psupertime_go_analysis* function and the specific gene profiles were plotted using the *plot_profiles_of_gene_clusters* function. Functional enrichment analysis was performed by Metascape.

Gene regulatory networks

The analysis of GRNs was performed by pySCENIC (v0.11.2) (Aibar et al., 2017) following the standard pipeline. In brief, gene co-expression modules were determined by *GRNboost2* implemented in the Arboreto package (v0.1.3). The GRNs were then inferred using pySCENIC, resulting in an area under the curve (AUC) score matrix representing the activity of each factor. GRNs were visualized using Cytoscape (v3.9.0).

Cell-cell interaction analysis

CellChat (v1.1.0) (Jin et al., 2021) was used to predict ligand-receptor interactions in the snRNA-seq data following standard procedure. Cell types containing fewer than 50 cells at any stage were excluded from further analysis. In brief, the expression matrix and cell type information were imported to CellChat. The overall communication probability among cell clusters was calculated using the *computeCommunProb* function with trim set to 0. The total number of interactions and interaction strength were obtained via the function *mergeCellChat*. Visualization of the differential number of interactions and interaction strength among different cell

populations was achieved using the function *netVisual_diffInteraction*.

RESULTS

Single-nucleus transcriptomic landscape of CCl_4-induced progressive liver fibrosis

To mimic the different clinical stages of human liver fibrosis, CCl_4 injections were administered to mice twice per week with repeated doses for up to 10 weeks. This model captures important properties of hepatoxic-induced human liver fibrosis, including inflammation, regeneration, and formation of fibrotic scars in a controllable manner (Ogaly et al., 2015). The extent of fibrosis was quantified using the Metavir scoring system based on Masson staining (Kim et al., 2017), confirming fibrosis expansion without septa (4.1% stained, early fibrosis stage) at 3 weeks (CCl_4-3w), fibrosis with a few septa (12.3% stained, moderate fibrosis stage) at 6 weeks (CCl_4-6w), and fibrosis with numerous septa (26.1% stained, advanced fibrosis stage) at 10 weeks (CCl_4-10w); fibrosis was absent in all corresponding vehicle groups (~0% stained, normal) (Figure 1A; Supplementary Figure S1A, B). Notably, compared with scRNA-seq of fresh tissues, snRNA-seq avoids the cellular stress induced by cell dissociation, which can perturb cell states, and facilitates the unbiased capture of cell populations, especially stromal cells (Han et al., 2022; Slyper et al., 2020; Zhang et al., 2022). Thus, we applied snRNA-seq to liver samples from two independent mice for each treatment (vehicle and CCl_4) at each time point (3 weeks, 6 weeks, and 10 weeks). After quality control, we obtained 49 919 nuclei (Vehicle-3w, 13 568 nuclei; CCl_4-3w, 5 136 nuclei; Vehicle-6w, 15 057; CCl_4-6w, 3 185 nuclei; Vehicle-10w, 11 087 nuclei; CCl_4-10w, 1 886 nuclei), with an average of 1 401 genes and 3 470 UMIs per nucleus (Supplementary Figure S1C). The reduced number of nuclei in the injured groups compared to the controls was related to the CCl_4-induced cell death under these conditions and the stringent cutoff for selecting nuclei (>2 000 UMIs) in our study. It should also be noted that during nucleus isolation, ambient RNA is often introduced into the suspension and retained in the droplets. However, the ambient RNA contamination rate in our data was 8.4% (Supplementary Figure S1D), which is lower than the moderate level (10%) described in other reports using snRNA-seq (Eraslan et al., 2022; Young & Behjati, 2020).

Uniform manifold approximation and projection (UMAP) and marker-based cell annotation led to the robust identification of 13 clusters corresponding to the main liver resident cell types across all conditions (Figure 1B–D; Supplementary Figure S1E, F), including: (1) hepatocytes, which could be further divided in pericentral (*Glul*$^+$), midzonal (*Hamp*$^+$), periportal (*Sds*$^+$), and cycling (*Mki67*$^+$) hepatocytes; (2) HSCs (*Reln*$^+$); (3) portal fibroblasts (*Aebp1*$^+$); (4) endothelial cells, including LSECs (*Kdr*$^+$) and liver vascular endothelial cells (LVECs, *Vwf*$^+$); (5) cholangiocytes (*Spp1*$^+$); and (6) relatively less abundant immune cell populations such as Kupffer cells (*Cd5l*$^+$), dendritic cells (*Siglech*$^+$), monocytes/non-Kupffer cell macrophages (*Ccr2*$^+$/*Gpnmb*$^+$), and T cells (*Il7r*$^+$). We failed to detect B cells, natural killer (NK) cells, or NKT cells, likely due to their low relative abundance.

ScRNA-seq has been applied previously to study CCl_4-induced liver fibrosis (Dobie et al., 2019; Filliol et al., 2022; Kostallari et al., 2022; Krenkel et al., 2019; Mederacke et al., 2022; Su et al., 2021; Terkelsen et al., 2020; Yang et al., 2021). However, these studies either focused on specific cell types (e.g., HSCs or endothelial cells) and/or analyzed a relatively restricted liver fibrosis time course. Our study provides an unbiased integrative (all major liver cell types) view of CCl_4-induced progressive liver fibrosis with temporal resolution, absent in previous studies. Differences between all datasets are depicted in Supplementary Table S1.

Hepatocyte transcriptomic responses during chronic CCl_4-induced liver injury

Liver fibrosis is accompanied by extensive hepatocyte death, compensatory proliferation, and severe metabolic dysfunction (Kisseleva & Brenner, 2021). Developing effective hepatocyte-protective drugs could elicit anti-fibrotic effects and reduce liver cirrhosis mortality (Roehlen et al., 2020). However, how hepatocytes react to injury at different stages of liver fibrosis is not yet well characterized, limiting the discovery of new therapeutic approaches.

To assess overall hepatocyte-specific gene expression patterns, we performed PCA of pseudobulk values for each hepatocyte subtype and condition in our dataset (Figure 2A). Results showed that hepatocytes in the control group were largely stable, whereas CCl_4 injury induced a shift in global gene expression in all hepatocyte subtypes, with a dramatic divergence between the early (CCl_4-3w) and late stages (CCl_4-6w and CCl_4-10w). To further explore these responses, we identified DEGs ($\log_2$ [fold-change]>0.25, Q<0.001) for all hepatocyte subtypes in the CCl_4-treated groups compared to the controls at each time point (Figure 2B; Supplementary Table S2). We observed stage-specific transcriptomic changes, especially at 3 weeks, with more than 79.5% of up-regulated genes and 52.2% of down-regulated genes being unique to this time point. Functional analysis of the up-regulated genes using Metascape (Zhou et al., 2019) revealed substantial enrichment of genes related to chromatin organization, cell cycle, signaling pathways such as Erbb and Wnt pathways, and embryonic morphogenesis, exclusively at 3 weeks (Figure 2C; Supplementary Figure S2A and Tables S3A, S4). Consistently, the expression levels of cell cycle-related genes (e.g., *Mki67*, *Top2a*, and *Cenpa*) were markedly increased in CCl_4-3w but less obviously in CCl_4-6w and CCl_4-10w (Figure 2D; Supplementary Tables S3A, S4). *Dnmt1*, *Dnmt3b*, and *Hdac3* were observed among the up-regulated chromatin regulators. Given that epigenetic control is involved in the regulation of liver regeneration (Macchi & Sadler, 2020; Wang et al., 2019), it is tempting to speculate that it also participates in hepatocyte proliferation and potentially other concomitant phenomena at the early stage of liver fibrosis. Likewise, the activation of embryonic morphogenesis-related genes (e.g., *Pou2f1* and *Prox1*) (Sebastiano et al., 2010; Zaret, 2002) suggests that hepatocytes undergo partial dedifferentiation to induce the proliferative program, as observed in other types of acute liver injury (Ben-Moshe et al., 2022; Chembazhi et al., 2021). In addition, the response to insulin and hormones, also linked to proliferation (Michalopoulos & Bhushan, 2021), was stronger at 3 weeks than at the later time points. The more substantially up-regulated genes at later stages included genes related to lipid biosynthesis, unfolded protein response, and complement activation (Figure 2C). Except for lipid biosynthesis, which was activated gradually, the other functions were exclusively boosted at 10 weeks. Of note, we observed no obvious changes when mapping these gene modules to the three main

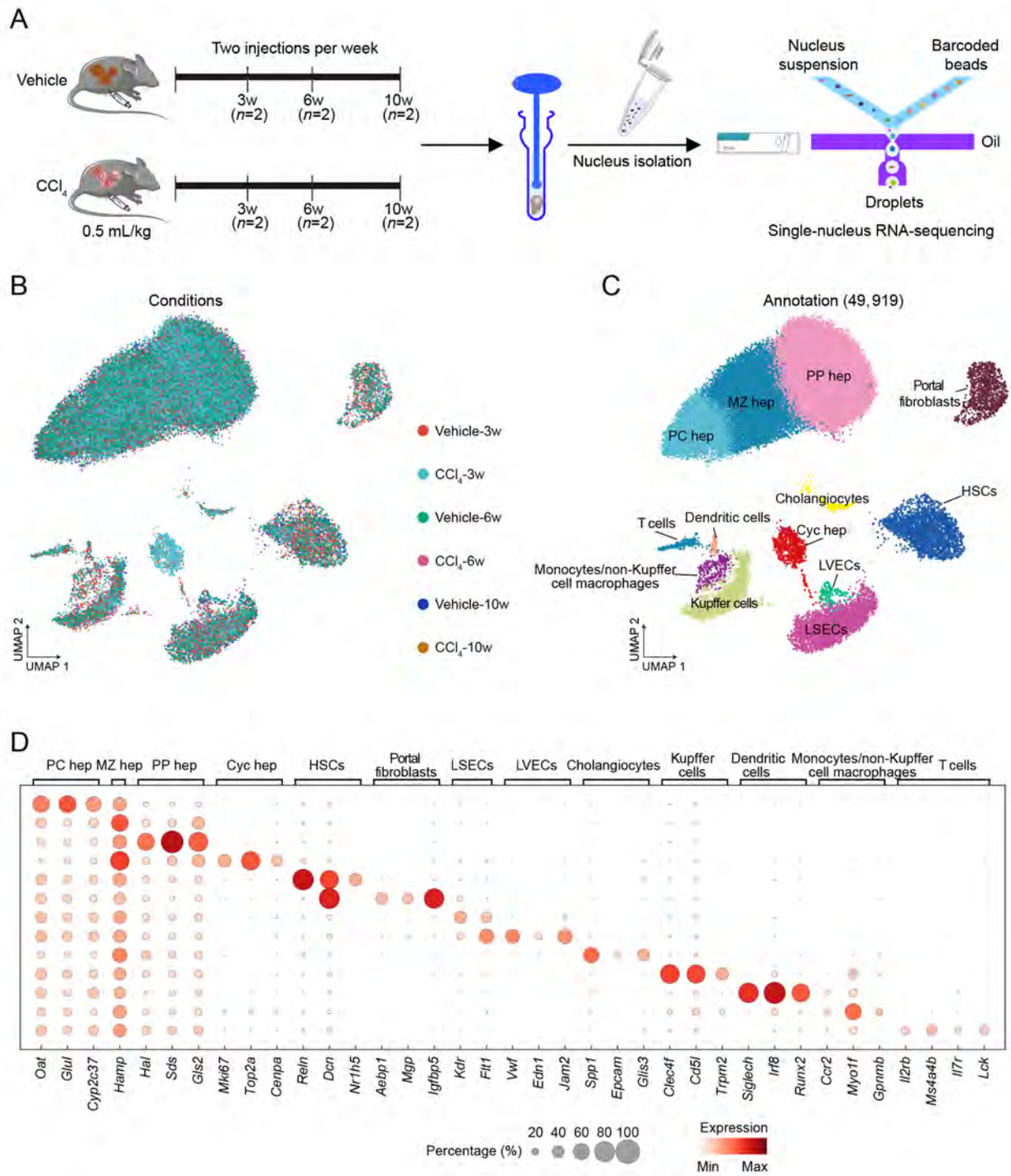

Figure 1 SnRNA-seq profiling of CCl_4-induced progressive liver fibrosis

A: Schematic overview of study design. Mice were subjected to intraperitoneal injections of CCl_4 for 3, 6, and 10 weeks to induce liver fibrosis. Control mice were treated with vehicle following the same time course. Animals (*n*=2) were sacrificed at selected time points and livers were extracted, snap frozen, and used for nuclear isolation for snRNA-seq library preparation. B: UMAP visualization of all profiled nuclei (*n*=49 919) colored by condition. C: UMAP visualization of all nuclei colored by cell type. PC hep, pericentral hepatocytes; MZ hep, midzonal hepatocytes; PP hep, periportal hepatocytes; Cyc hep, cycling hepatocytes; HSCs, hepatic stellate cells; LSECs, liver sinusoidal endothelial cells; LVECs, liver vascular endothelial cells. D: Bubble plot showing expression levels of each canonical marker in the indicated cell types.

hepatocyte subtypes (pericentral, midzonal, and periportal) (Supplementary Figures S2B, C; Supplementary Table S4). Altogether, these changes point to a higher burden of cell stress and proliferation exhaustion at the late fibrosis stage.

For the down-regulated genes, we observed enrichment in metabolic-related pathways (e.g., epoxygenase P450, arachidonic acid metabolic, and long-chain fatty acid metabolic process) at 3 weeks, which became more obvious with continuing fibrosis, indicating progressively exacerbated metabolic dysfunction (Figure 2C, E; Supplementary Figure S2D and Tables S3A, S4). This was exemplified by the reduced expression of cytochrome P450 family genes (e.g.,

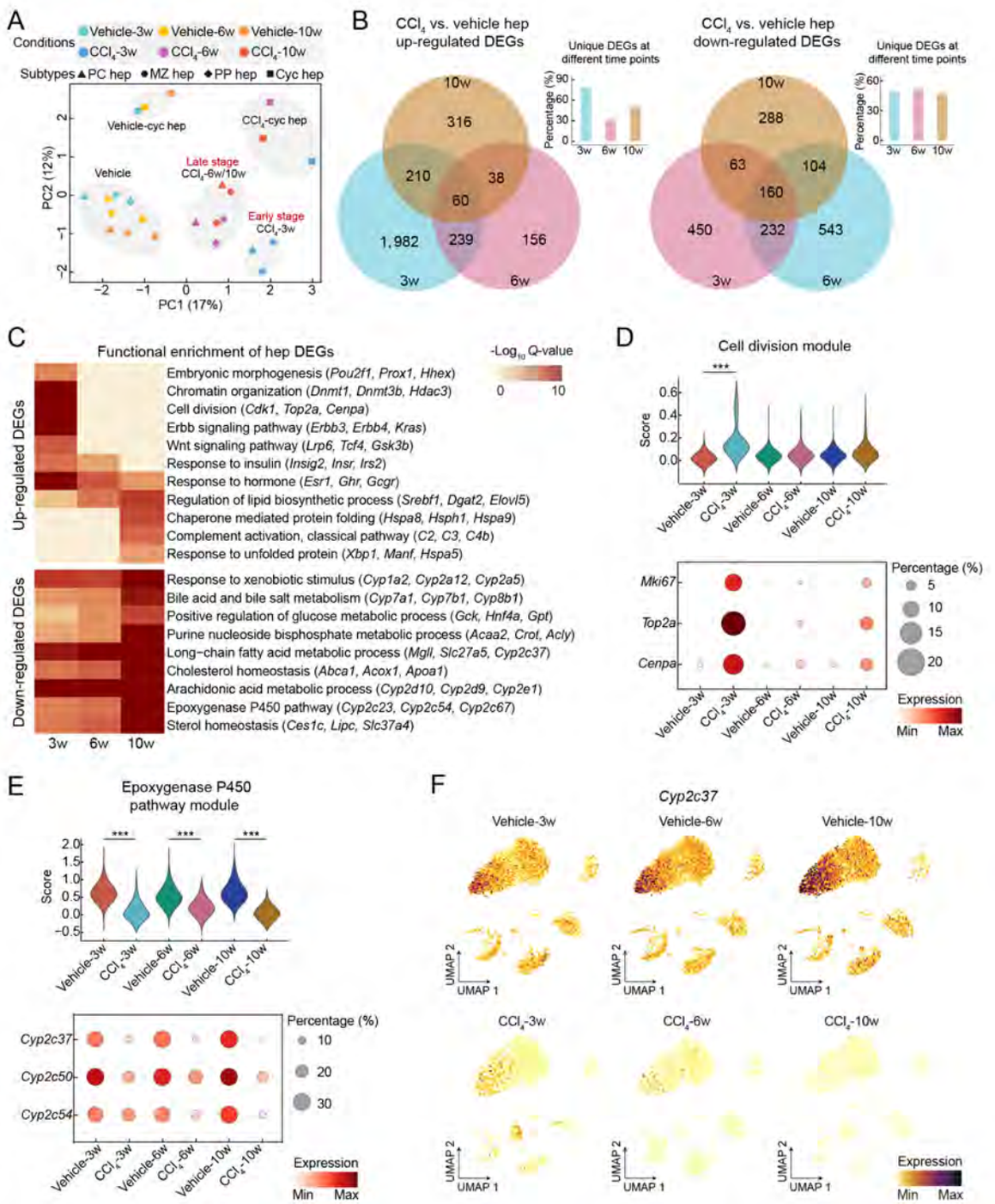

Figure 2 SnRNA-seq analysis of hepatocyte responses at different fibrosis stages

A: PCA of pseudobulk data of hepatocytes from each condition. Color represents different conditions and shape represents hepatocyte subtypes. B: Venn diagram showing overlap between up-regulated (left) and down-regulated (right) genes in hepatocytes at each time point comparing CCl_4-treated group to the corresponding vehicle control group, with percentage of unique DEGs for each time point shown as bar plots. C: Heatmap showing functional enrichment (calculated using Metascape (Zhou et al., 2019)) associated with up-regulated (upper) and down-regulated (bottom) genes obtained from hepatocytes at each time point comparing CCl_4-treated group to the corresponding vehicle control group. Representative genes related to the corresponding pathways are indicated on the right side. Benjamini-Hochberg corrected *P*-values. D: Top: violin plot showing module scores for the cell division module in different conditions. Bottom: bubble plot showing expression levels of cell cycle-related genes (*Mki67*, *Top2a*, and *Cenpa*) in hepatocytes for the indicated conditions. *P*-values were calculated using Wilcoxon rank sum test. ***: $P<0.001$. E: Top: violin plot showing module scores for the epoxygenase P450 pathway in hepatocytes for each condition. Bottom: bubble plot showing expression levels of epoxygenase P450 pathway-related genes (*Cyp2c37*, *Cyp2c50*, and *Cyp2c54*) in hepatocytes for the indicated conditions. *P*-values were calculated using Wilcoxon rank sum test. ***: $P<0.001$. F: UMAP visualization of expression level of *Cyp2c37* in the indicated conditions.

Cyp2c37, *Cyp2c50*, and *Cyp2c54*). Importantly, metabolic perturbation was mostly restricted to pericentral hepatocytes (Figures 2F; Supplementary Figure S2E and Table S4), consistent with the fact that CCl_4 is a classical pericentral

hepatotoxicant (Chen et al., 2020). Immunofluorescence for glutamine synthetase confirmed the reduction in pericentral metabolic functions in our experimental settings (Supplementary Figure S2F).

These findings provide new insights into the dynamic responses of hepatocytes in CCl_4-induced progressive liver fibrosis.

Molecular roadmap of hepatic stellate cell activation at different fibrosis stages

HSCs are the major source of ECM-producing myofibroblast-like cells, also termed aHSCs, in hepatoxic-induced fibrosis (Kisseleva & Brenner, 2021). The clearance of aHSCs is considered a key strategy for liver fibrosis resolution (Tsuchida & Friedman, 2017), but how HSC activation and clearance are modulated at different fibrosis stages remains incompletely understood.

To study the molecular dynamics of HSC activation during CCl_4-induced progressive liver fibrosis, we first reconstructed their trajectory in CCl_4-treated mice using Monocle2 (Qiu et al., 2017). The resulting pseudotime trajectory recapitulated the progression of HSCs from the quiescent (qHSC) to aHSC state (*Col1a1* and *Col1a2*), with HSCs in the CCl_4-treatment groups predominantly displaying the aHSC phenotype (Figure 3A; Supplementary Figure S3A). One caveat to this approach is that Monocle2-based pseudotime trajectory tends to overfit specific processes into a single trajectory, which may complicate distinguishing aHSCs with potential asynchrony at the early and late stages of liver fibrosis.

We predicted that aHSCs may be further classified into distinct molecular subsets due to prolonged exposure to environmental stress as fibrosis progresses from the mild to severe stages. Thus, we performed psupertime analysis (Macnair et al., 2022), a supervised pseudotime approach based on a regression model that explicitly uses time-series labels as input. This improves classification accuracy and identification of genes with coherent expression patterns along a time series. Based on the combined 2 740 DEGs between the CCl_4-treatment and control groups at each time point ($\log_2$ [fold-change]>0.25, Q<0.001) (Supplementary Table S5), we discriminated HSCs into three progressive cell states with continuing fibrosis (Figure 3B). The qHSC state was detected exclusively in the Vehicle-3w group. The early-aHSC (E-aHSC) state was mainly composed of HSCs at the early fibrosis stage (CCl_4-3w), although some cells at this stage had entered a late-aHSC (L-aHSC) state. Most HSCs at the late fibrosis stage (CCl_4-6w and CCl_4-10w) were enriched in L-aHSCs. Along this psupertime-based trajectory, we observed four main clusters of genes displaying distinct expression patterns and functions (Figure 3C–F; Supplementary Table S3B). Cluster 1 (n=291) consisted of genes with high expression in qHSCs, decreasing along the activation trajectory. This cluster was enriched in retinol metabolism (e.g., *Rdh7* and *Rbp4*), a major metabolic feature of qHSCs (Lee & Jeong, 2012), indicating a loss of qHSC identity. The *Mbl1* and *Mbl2* genes, which correspond to pattern-recognition molecules and MHC class I genes *H2-K1* and *H2-Q10*, were also in this cluster. Their reduction may help avoid excessive lymphocyte activation by reducing the presentation of antigens produced by necrotic hepatocytes, as observed in mouse liver after acute acetaminophen intoxication (Ben-Moshe et al., 2022). Cluster 2 (n=767) genes were up-regulated in E-aHSCs and mostly corresponded to chromatin organization (e.g., SWI/SNF chromatin remodeling complex subunit *Arid1a* and histone demethylase *Kdm2a*). Although epigenetic mechanisms play a role in HSC activation during liver fibrosis (Barcena-Varela et al., 2021), our analysis suggests that this is more critical at the early fibrosis stage, as these genes return to baseline levels at the late stage. NADPH oxidase 4 (*Nox4*), a transmembrane enzyme that generates reactive oxygen species (ROS) to promote HSC activation (Aoyama et al., 2012; Lan et al., 2015), was also enriched in cluster 2. Related to this, E-aHSCs displayed high levels of p38α (*Mapk14*), which facilitates HSC activation in an oxidative stress-dependent manner (Cao et al., 2002). A transient oxidative stress response in E-aHSCs was further supported by the induction of antioxidant response factors, such as *Gclc*, *Txnrd1*, and *Nfe2l2*, at CCl_4-3w. Cluster 3 (n=98) was composed of genes exclusively activated in L-aHSCs, including the anti-apoptotic factors *Bcl2* and *Tnfrsf11b* (osteoprotegerin). The latter is a soluble decoy receptor for the tumor necrosis factor (TNF)-related apoptosis inducing ligand (TRAIL), competing with TRAIL binding to death receptors to prevent aHSC apoptosis. Indeed, high levels of *Tnfrsf11b* have also been detected in CCl_4-induced late murine liver fibrosis and human cirrhotic liver (Adhyatmika et al., 2020). Supporting this, the apoptosis activators *Fas* and *Casp8* were transiently induced in E-aHSCs, suggesting that aHSC clearance by apoptosis is more effective at the early fibrosis stage. Inhibition of osteoprotegerin may thus be of clinical relevance for inducing aHSC apoptosis in late liver fibrosis. Cluster 4 (n=1 584) consisted of genes that continuously increased from qHSCs to L-aHSCs. Apart from genes related to collagen formation and ECM organization (e.g., *Col3a1*), we observed enrichment of chemotaxis factors (e.g., *Csf1*) and pro-fibrogenic signaling (Tsuchida & Friedman, 2017) driven by PDGF (e.g., *Pdgfrb*), TGFβ (e.g., *Tgfbr1*), and Hippo signaling (e.g., *Tead1*), indicating a stepwise enhancement of HSC activation.

To verify our observations, we retrieved previously published data from a scRNA-seq study of HSC activation in a murine 3-week CCl_4 injury model (Yang et al., 2021) and a CCl_4 injury model induced from a single injection to up to 19 injections (one injection every 3 days, around 8 weeks) (Filliol et al., 2022; Mederacke et al., 2022) (Supplementary Figure S3B–G and Table S4). By integrating these datasets, we confirmed the reduction in immune modulation function and induction of pro-apoptotic factors at the early fibrosis stage, as well as the accumulation of ECM-related pathways and pro-fibrotic signals during progressive liver fibrosis. Interestingly, we also observed a transient reduction in anti-apoptotic factors after 4 and 12 CCl_4 injections and a slight reactivation afterwards (19 injections), which did not reach the level of CCl_4-10w in our dataset, supporting that dysfunction in the clearance by apoptosis in aHSCs occurs exclusively at the advanced fibrosis stage.

We concluded that HSC activation in CCl_4-induced progressive liver fibrosis is a multistage process coordinated by diverse factors and signaling networks, with disruption of apoptotic regulation.

Dynamics of angiogenic responses at different fibrosis stages

Upon chronic liver injury, LSECs lose their fenestrae and become capillarized, which involves the development of a thick basement membrane to form a continuous endothelium

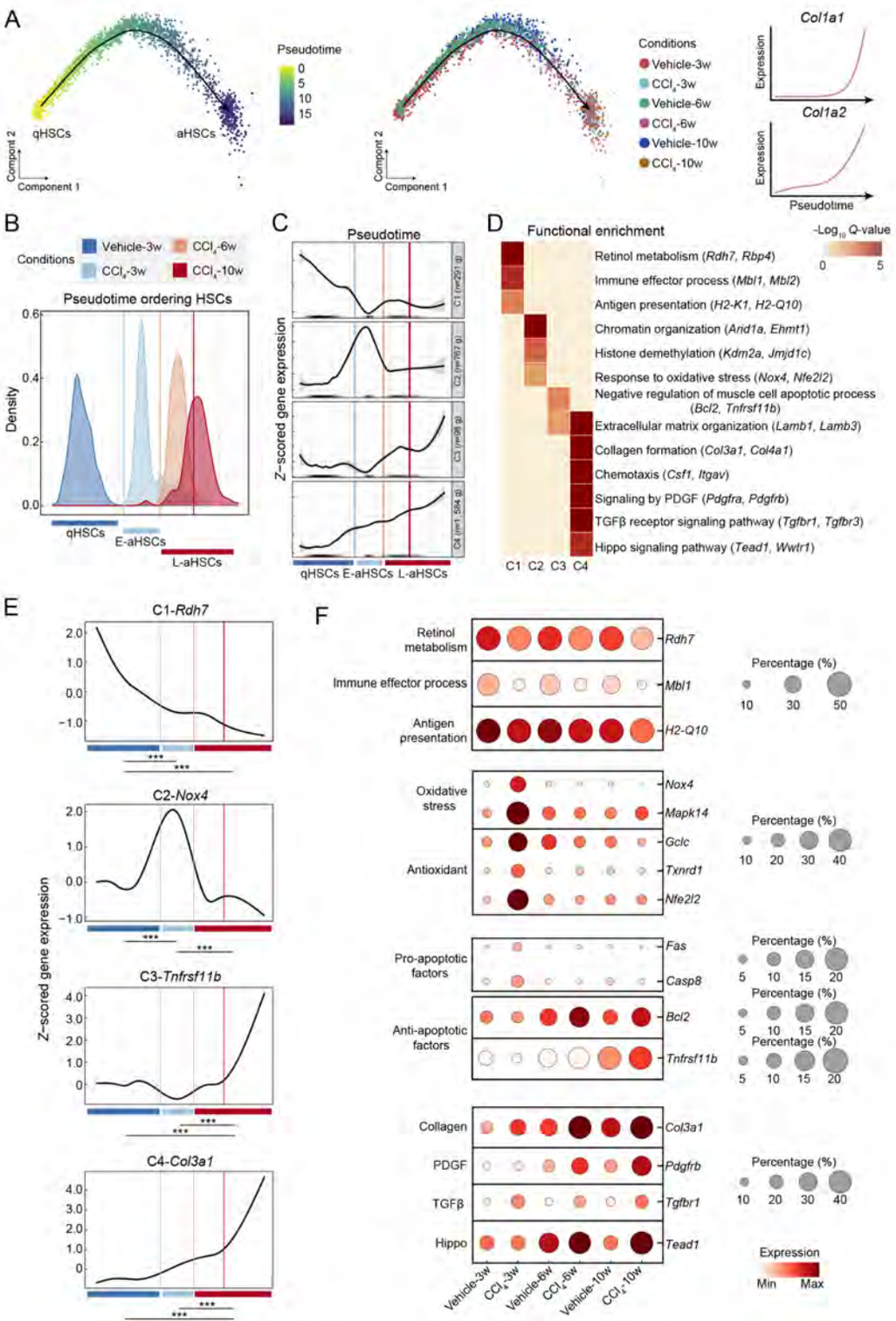

Figure 3 SnRNA-seq analysis of HSC activation kinetics at different fibrosis stages

A: Left: Monocle2-based trajectory reconstruction of HSC activation during liver fibrosis, colors represent pseudotime (left) or conditions (right). Right: expression of aHSC marker genes (*Col1a1* and *Col1a2*) along Monocle2-based pseudotime trajectory. qHSCs, quiescent HSCs; aHSCs, activated HSCs. B: Psupertime histogram representation of HSCs classified as qHSCs, E-aHSCs, and L-aHSCs. Vertical lines indicate thresholds for distinguishing adjacent state learned by psupertime. E-aHSCs, early-activated HSCs; L-aHSCs, late-activated HSCs. C: Psupertime clustering of 2 740 DEGs in HSCs between CCl_4-treated and control groups at each time point, identifying four gene clusters with different gene expression dynamics. Vertical lines indicate thresholds for distinguishing adjacent state learned by psupertime. D: Heatmap showing functional enrichment results performed by Metascape for each gene cluster. Representative genes related to the corresponding pathways are indicated on the right side. Benjamini-Hochberg corrected *P*-values. E: Line charts showing expression levels of representative genes for the indicated gene clusters; cells were ordered by psupertime-based pseudotime. *P*-values were calculated by Wilcoxon rank sum test. ***: $P<0.001$. F: Bubble plots showing expression levels of selected genes related to the indicated pathways in HSCs for each condition.

(Lafoz et al., 2020; Poisson et al., 2017). This capillarization contributes to sustaining HSC activation and liver dysfunction. When injury progresses further, pathological angiogenesis is induced, which, in turn, aggravates fibrosis. Understanding this process may help develop rational approaches for improving ultimate clinical outcomes.

To systematically dissect LSEC responses at different fibrosis stages, we again performed psupertime-based pseudotime analysis with our snRNA-seq time course. Based on the distinct molecular programs across different CCl_4-induced liver fibrosis stages, LSECs were divided into three cell states, including homeostatic LSECs (hLSECs) in the vehicle group, early-response LSECs (E-rLSECs) in CCl_4-3w, and late-response LSECs (L-rLSECs) enriched in CCl_4-6w and CCl_4-10w (Figure 4A). Along this trajectory, we identified four main gene clusters with distinct expression patterns and functions (Figure 4B–E; Supplementary Tables S3C, S6). Expression of genes in cluster 1 (n=324) decreased along the trajectory, with enrichment in homeostatic LSEC functions, as expected, including the regulation of complement activation (e.g., *Serping1*) and endocytosis (e.g., *Scarb2*) (Su et al., 2021). Cluster 2 (n=1 690) was composed of genes transiently up-regulated in E-rLSECs and was enriched in p53 signaling (e.g., *Cdkn1a*), Notch signaling (e.g., *Notch2* and *Rbpj*), and negative regulation of angiogenesis (e.g., *Stard13*). Notch signaling in endothelial cells down-regulates the expression of pro-angiogenic receptors (e.g., VEGFR2/3) to suppress sprouting angiogenesis (Benedito et al., 2009). *Cdkn1a* (p21) induces cell cycle arrest to prevent or terminate angiogenesis (Mühleder et al., 2021), whereas *Stard13* (DLC2) is a negative regulator of angiogenic responses in endothelial cells by modulating cell attachment and migration (Lin et al., 2010). These findings indicate the existence of an overall response to counteract the onset of angiogenesis at the early fibrosis stage. Genes in cluster 3 (n=56) were transiently down-regulated in E-rLSECs but strongly induced in L-rLSECs. These genes were largely related to VEGFR signaling, including *Flt4* (VEGFR3) and *Nrp2* (neuropilin-2), as well as sprouting angiogenesis factors, such as *Pecam1* and *Robo4* (Mühleder et al., 2021), indicating elevated pathological angiogenesis at the late fibrosis stage. Epidermal growth factor-like protein 7 (*Egfl7*), an antagonist of Notch signaling (Schmidt et al., 2009), was also enriched in cluster 3, indicating that the Notch-VEGFR axis may differentially modulate angiogenesis across various fibrosis stages. The increase in *Egfl7* at the late fibrosis stage has not been reported previously and was confirmed by smFISH (Figure 4F). Genes in cluster 4 (n=2 486) gradually increased during liver fibrosis and were enriched in ECM-receptor interactions, cell adhesion, and LSEC capillarization (e.g., *Vwf* and *Cd34*) (Su et al., 2021), representing an accumulated pathological LSEC response to chronic CCl_4-induced liver injury.

Thus, we identified new mechanisms of LSEC capillarization and angiogenesis as CCl_4-induced liver fibrosis progresses towards the late stage, clarifying how vascular responses contribute to liver dysfunction in this setting.

Cell-cell communication networks during progressive liver fibrosis

Prolonged hepatoxic injury disrupts microenvironment homeostasis, leading to severe changes in intercellular interactions (Tsuchida & Friedman, 2017). Reversing this process is considered an important strategy for tackling the molecular events that lead to liver fibrosis. To explore the dynamic changes in intercellular crosstalk that orchestrate the progression of CCl_4-induced liver fibrosis, we applied CellChat (Jin et al., 2021) to our time course dataset. To facilitate calculations, the CCl_4-6w and CCl_4-10w groups were combined as the late fibrosis stage, while all vehicle groups at different time points were pooled together as the control. Total number of interactions was slightly reduced at the early fibrosis stage but substantially increased at the late stage (Figure 5A; Supplementary Table S7). The most extensive boost at the late stage was observed in HSCs (Figure 5B; Supplementary Figure S4A), in line with their more substantial activation at this time point.

We then specifically assessed the cellular communication networks governing HSC activation by extracting the expression of ligands from all cell types and their corresponding receptors in HSCs in all conditions (Figure 5C; Supplementary Figure S4B). As expected, there was a general increase in canonical pro-fibrogenic PDGF (e.g., *Pdgfa*, *Pdgfc*, and *Pdgfd*) and TGFβ signaling (e.g., *Tgfb1*, and *Tgfb2*) ligands, mainly contributed by HSCs, portal fibroblasts, cholangiocytes, and Kupffer cells in the CCl_4 groups, as well as their corresponding receptors (*Pdgfra*/*b* and *Tgfbr1/2*) in HSCs, consistent with the well-established role of these pathways in liver fibrosis. In addition, we observed a transient up-regulation in the expression of neuregulin signaling ligands (*Nrg1* and *Nrg3*) in multiple cell types and their corresponding receptors (*Erbb3* and *Erbb4*) in HSCs in CCl_4-3w. A similar pattern was observed for class III semaphorin factors *Sema3a* and *Sema3e*, which are mainly expressed in HSCs and portal fibroblasts, and their receptors (*Nrp1*, *Plxna2*, and *Plxna4*) in HSCs. Although neuregulin-1 and semaphorin-3E have previously been implicated in liver fibrosis (Yagai et al., 2014), our results suggest that they may only act during a specific time window.

Next, we explored the crosstalk between LSECs and other cell types to reveal additional angiogenesis-related interactions (Figure 5D; Supplementary Figure S4B). *Vegfc* and *Vegfd* but not *Vegfa* were boosted in both CCl_4 groups, with *Vegfc* activated at a constant level in all CCl_4 groups and *Vegfd* mostly at the early fibrosis stage. However, among the corresponding receptors, only the VEGFC/VEGFD receptor VEGFR3 (*Flt*4) was induced at a higher level in late fibrosis. The up-regulation of VEGFR3 may help explain why anti-VEGFR2 treatment alone has only a mild therapeutic effect in advanced fibrosis (Liu et al., 2017). In addition to VEGFs, angiopoietin signaling is an important angiogenesis regulator (Carmeliet & Jain, 2011). *Angpt1*, mainly expressed in HSCs, but not *Angpt2*, was increased in all CCl_4 groups, whereas their receptor *Tek* (TIE2) was more substantially induced in LSECs at the late fibrosis stage.

We also observed an increase in the expression of macrophage colony stimulating factor (*Csf1*) expressed in HSCs and portal fibroblasts, especially at the late fibrosis stage (Supplementary Figure S4B). CSF1 interacts with CSF1R in Kupffer cells and induces their accumulation in liver fibrosis (Liu et al., 2010; Stutchfield et al., 2015) (Supplementary Figure S4C). This is consistent with Kupffer cells being the main source of fibrinolytic matrix metalloproteinases as a compensatory mechanism to remove fibrosis (Kisseleva & Brenner, 2021). In this regard, we detected increased expression of *Mmp12* and *Mmp14* in

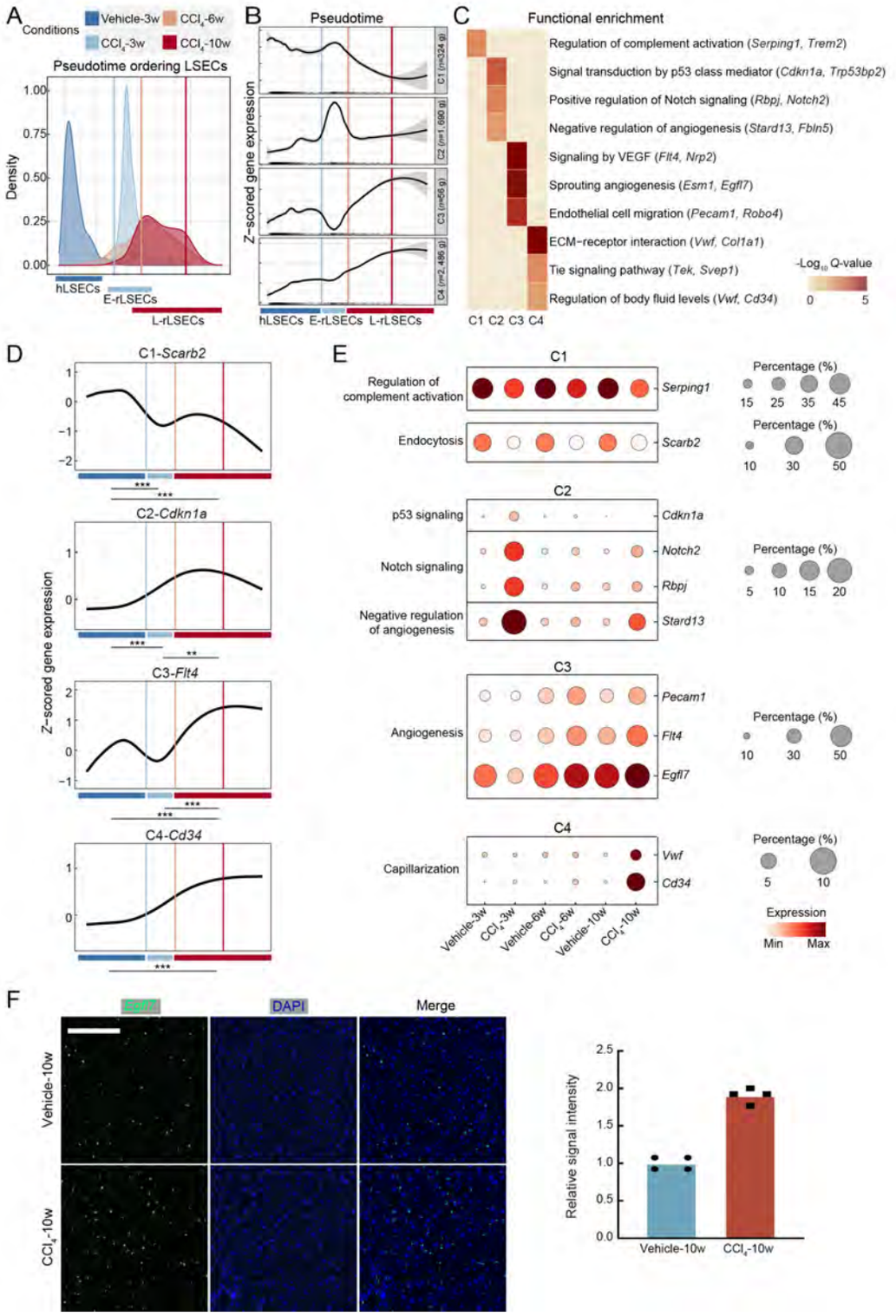

Figure 4 SnRNA-seq analysis of molecular dynamics of vascular responses at different fibrosis stages

A: Psupertime histogram of LSECs classified as hLSECs, E-rLSECs, or L-rLSECs. Vertical lines indicate thresholds for distinguishing adjacent state learned by psupertime. hLSECs, homeostatic LSECs; E-rLSECs, early-response LSEC; L-rLSECs, late-response LSECs. B: Psupertime clustering of 4 556 DEGs in LSECs between CCl_4-treated and control groups at each time point, identifying four gene clusters with different gene expression dynamics. Vertical lines indicate thresholds for distinguishing adjacent state learned by psupertime. C: Heatmap showing functional enrichment results performed by Metascape for each gene cluster. Representative genes related to the corresponding pathways are indicated on the right side. Benjamini-Hochberg corrected *P*-values. D: Line charts showing expression levels of representative genes for the indicated gene clusters; cells were ordered by psupertime-based pseudotime. *P*-values were calculated by Wilcoxon rank sum test. **: $P<0.01$; ***: $P<0.001$. E: Bubble plots showing expression levels of selected genes related to the indicated pathways in LSECs for each condition. F: Left: representative images of smFISH staining for *Egfl7* (green) and DAPI (blue) performed in Vehicle-10w and CCl_4-10w sections. Scale bar: 100 μm. Right: quantification of signal intensity for *Egfl7* from four different random fields.

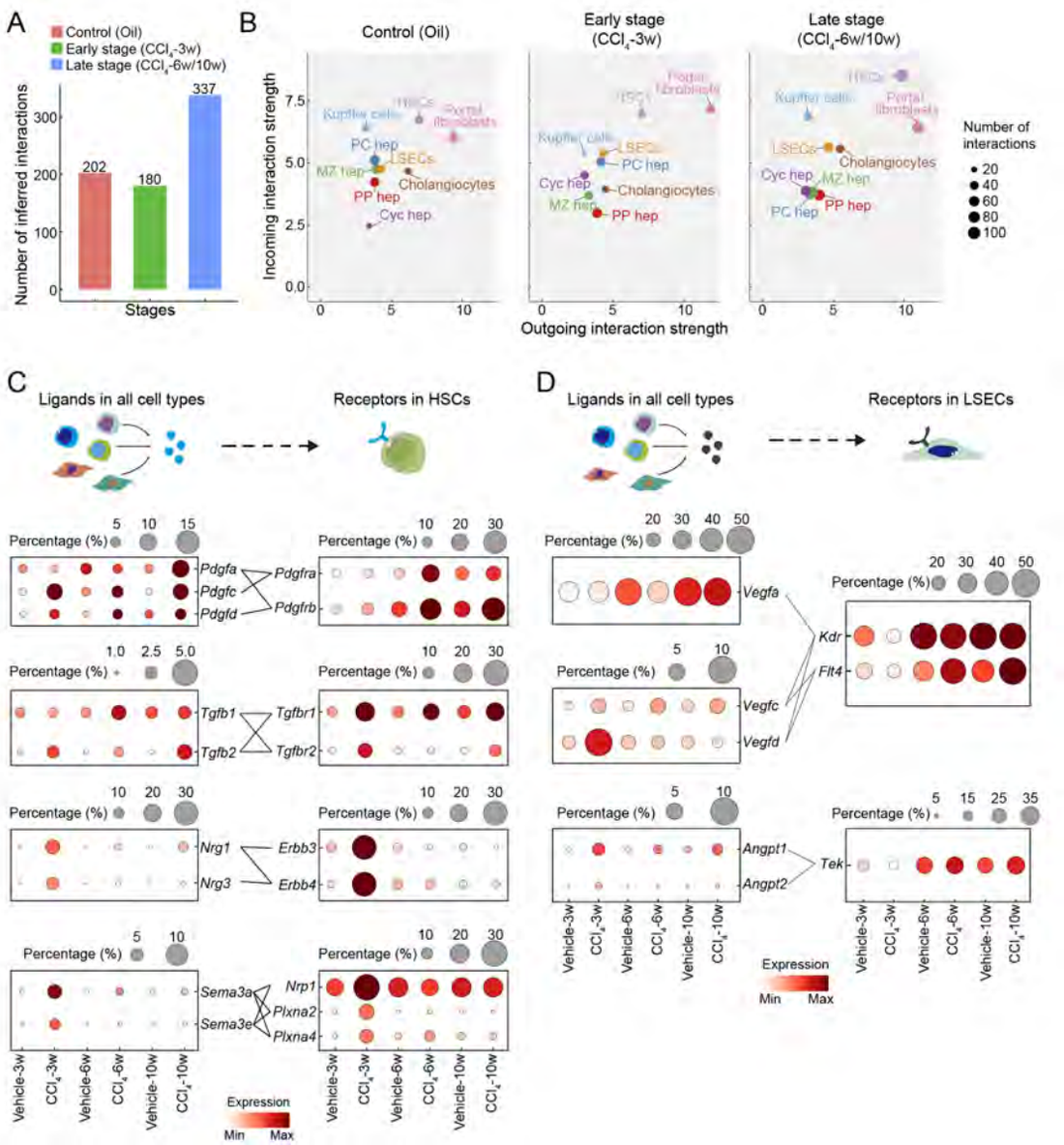

Figure 5 SnRNA-seq analysis of dynamics of cell-cell communication networks at different fibrosis stages

A: Bar plot showing the number of inferred interactions identified in vehicle and CCl_4 treatment groups. B: Dot plot showing outgoing (ligand) and incoming (receptor) interaction strength measured by CellChat for each cell type in vehicle and CCl_4 treatment groups. Dot size represents number of inferred interactions in each cell type. C: Top: schematic of ligands interacting with their corresponding receptors in HSCs. Bottom: bubble plots showing expression levels of ligands in all cell types (left) and the corresponding receptors in HSCs (right) for indicated conditions. D: Top: schematic of ligands interacting with corresponding receptors in LSECs. Bottom: bubble plots showing expression levels of ligands in all cell types (left) and corresponding receptors in LSECs (right) for indicated conditions.

Kupffer cells at the late fibrosis stage (Supplementary Figure S4D).

Our detailed characterization of the dynamic microenvironment crosstalk helps understand how cell-specific responses are regulated at different stages of CCl_4-induced progressive liver fibrosis.

Cell-specific gene regulatory networks during progressive liver fibrosis

Transcription factors and their cofactors regulate the expression of each other and their downstream target genes and are essential for controlling cell state transitions (Wagner et al., 2016). The SCENIC algorithm (Aibar et al., 2017; Dai et al., 2020) can be used to examine GRNs in sc/snRNA-seq datasets, which predicts the activity of each transcription factor/cofactor (regulons) by integrating co-expression modules between them and their candidate target genes (Figure 6A). Here, we applied the SCENIC algorithm to our time course snRNA-seq dataset to dissect the key regulators driving cell state transitions in different cell types during CCl_4-induced progressive liver fibrosis. In total, we identified 258 active regulons, with 41 active in hepatocytes, 58 active in HSCs, and 53 active in LSECs (scaled AUC>0.3; Supplementary Table S8).

We first explored the regulons in hepatocytes at different fibrosis stages and observed regulons with distinct kinetics (Figures 6B–D). In the CCl_4-3w group, transiently up-regulated regulons included SOX5 and ZEB1 in all hepatocyte subtypes, which may be responsible for inducing a partial epithelial-to-mesenchymal transition (Wang et al., 2015), consistent with

the above evidence suggesting partial dedifferentiation (see Figure 2C and Supplementary Figure S2A). In this regard, upon acetaminophen injury, hepatocytes located at the interface between damaged and nondamaged areas gain a mesenchymal-like shape (Ben-Moshe et al., 2022). Although we did not observe a distinct cluster of specialized hepatocytes corresponding to these cells, their existence cannot be excluded in response to CCl_4 treatment, which warrants further evaluation using spatially resolved technologies (Chen et al., 2022). We also detected the oncoprotein MYB family factor MYBL1 and epigenetic modifiers EZH2 and KDM5A with minimal differences among hepatocyte subtypes (Supplementary Figure S5A). EZH2 is associated with active hepatocyte proliferation (Bae et al., 2015). Consistently, gene targets of these five regulons were enriched in developmental growth, mitotic cell cycle, and chromatin organization. Likewise, lipid synthesis regulator SREBF1 (Xu et al., 2023) showed a strong up-regulation in the CCl_4-10w group, and functional enrichment of the downstream gene targets for this regulon confirmed its regulatory effects on lipid biosynthesis. The down-regulated regulons in the CCl_4 groups at all time points included the PPAR signaling factor PPARG, xenobiotic detoxification regulator DBP, and retinoid X receptor RXRA, which were enriched in pericentral hepatocytes (Supplementary Figure S5A). As expected, the downstream target genes of these regulons were mostly related to pericentral metabolic functions, such as xenobiotic metabolism, PPAR signaling, and primary bile acid biosynthesis (Halpern et al., 2017). These findings help explain the pericentral metabolic dysfunction observed in CCl_4-induced injury. Of note, DBP is also involved in the regulation of circadian rhythms (Gachon et al., 2006), suggesting disruption in the circadian clock upon CCl_4 injury. Supporting this, the expression levels of other key circadian rhythm regulators (e.g., *Bmal1*, *Clock*, and *Npas2*) were highly perturbed (up-/down-regulated) in the CCl_4-treatment groups (Supplementary Figure S5B), especially at 3 weeks. These findings are consistent with the fact that circadian rhythm disorganization exacerbates liver diseases and vice versa (Tahara & Shibata, 2016).

Next, we studied the GRNs in HSCs that may be involved in regulating their activation and identified several regulons with increased activity as fibrosis progressed (Figure 6E–G). These included AP-1 family transcription factors (FOS, FOSL2, and JDP2), YAP signaling co-factor TEAD1, and MEF2C (myocyte enhancer factor 2C), which are known to orchestrate HSC activation (Kisseleva & Brenner, 2021; Mannaerts et al., 2015; Zhang et al., 2019). In general, the downstream gene targets of these regulons were enriched in ECM organization and regulation of cell motility, consistent with the characteristics of aHSCs. In addition, ATF3 and RELB were enriched at the late fibrosis stage. The former is related to endoplasmic reticulum stress and the latter is a member of the NF-κB family. In this regard, inhibiting NF-κB signaling activity can lead to aHSC apoptosis and resolution of liver fibrosis (Kisseleva & Brenner, 2021).

We also explored the GRNs in LSECs (Supplementary Figure S5C–E) and identified increased activity in a series of pro-angiogenic ETS family transcription factors (ETS1/2, ELF4, SPI1, SPIB, and SPIC) (Oettgen, 2010) as fibrosis progressed into the late stage. We also detected RUNX1 and WT1, with the former implicated in aberrant retinal angiogenesis (Lam et al., 2017) and the latter a major regulator of tumor angiogenesis (Wagner et al., 2014).

In summary, our analysis reconstructed the GRNs controlling cell type-specific responses in CCl_4-induced progressive liver fibrosis.

DISCUSSION

To understand the dynamics of progressive liver fibrosis, we have generated a single-cell atlas covering 49 919 cells in a mouse model of CCl_4-induced injury, providing a powerful resource for identifying stage-specific multicellular responses and the underlying intercellular interaction networks (Figure 7).

Using this approach, we studied the mechanisms of compensatory hepatocyte proliferation after injury and found that this capacity gradually became exhausted as fibrosis progressed into the late stage. We also provide a roadmap of how accumulating CCl_4 injury can lead to disruption in pericentral metabolic function. Interestingly, we found that chromatin regulators exhibited significant changes in hepatocyte expression at the early stage of fibrosis. This phenomenon may contribute to the onset of hepatocyte proliferation and metabolic remodeling, suggesting that modulation using small molecules may help improve these changes.

In addition to the classical division of HSCs into qHSC and aHSC states, we classified aHSCs into E-aHSCs and L-aHSCs, with the latter showing substantial enrichment in late-stage fibrosis. Similarly, previous research identified different subpopulations of HSCs in fibrotic livers, with the HSC subtype with stronger myofibroblast signatures supporting hepatocellular carcinoma development (Filliol et al., 2022). Interestingly, we found that anti-apoptotic factors, including *Bcl2* and *Tnfrsf11b*, were more enriched in L-aHSCs, indicating that the apoptotic clearance mechanism of aHSCs may be dysfunctional at this stage. This suggests that anti-*Tnfrsf11b* treatment (e.g., with antibodies) may be beneficial in this setting, as supported by the inverse association between HSC apoptosis and fibrosis in chronic hepatitis C virus infection (Gonzalez et al., 2009). Furthermore, L-aHSCs exhibited elevated levels of factors involved in classic fibrogenic signaling pathways, including the TGFβ, PDGF, and Hippo pathways (Tsuchida & Friedman, 2017). Likewise, we observed several factors involved in HSC activation that only appeared transiently at the early fibrosis state, such as *Nox4*, which enhances ROS generation to accelerate HSC activation (Tsuchida & Friedman, 2017). *Nox1/4* knockout or treatment with the NOX1/4 inhibitor GKT137831 improves liver fibrosis in mice (Aoyama et al., 2012; Lan et al., 2015), although their effects have only been evaluated for 3–6 weeks after CCl_4 injury. Given the low expression of *Nox1/4* at late-stage fibrosis, it is conceivable that inhibiting NOX1/4 in cirrhotic livers will have no beneficial effect.

Our results also showed that the level of capillarization in LSECs cumulatively increased during liver fibrosis progression. Furthermore, anti-angiogenic factors such as *Cdkn1a*, *Rbpj*, and *Stard13* were transiently activated during early-stage fibrosis to restrain the onset of pathological angiogenesis. Correspondingly, pro-angiogenic signaling factors were down-regulated in early-stage fibrosis but became strongly activated later. As Notch activation represses VEGFR2/3 expression (Benedito et al., 2009), up-regulation of EGFL7, a Notch antagonist, during late-stage fibrosis may be involved in the biphasic behavior of VEGFR2/3. Overall, these findings imply that pathological angiogenesis is

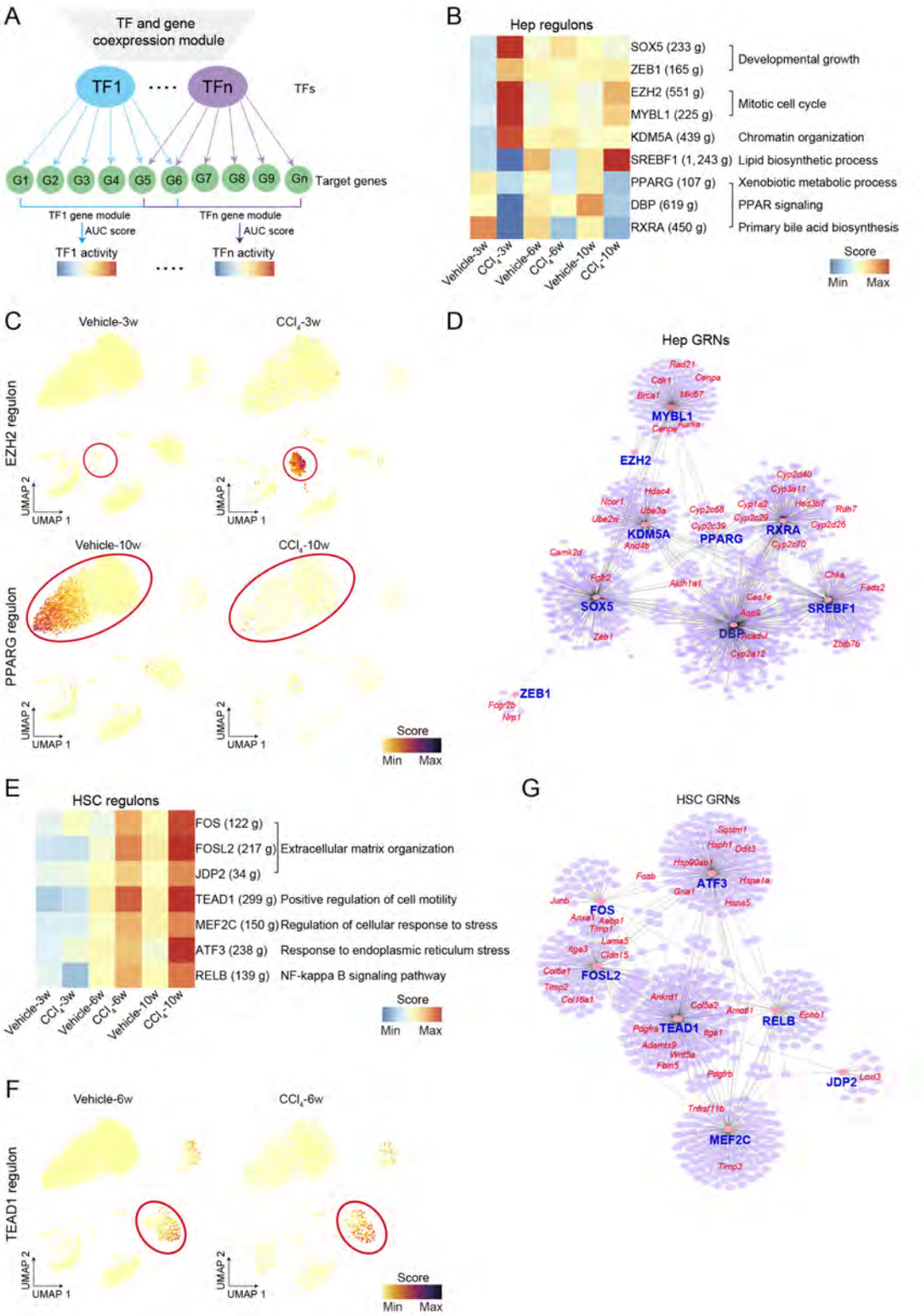

Figure 6 SnRNA-seq analysis of gene regulatory dynamics in hepatocytes and HSCs at different fibrosis stages

A: Schematic of SCENIC workflow. Transcription factor/cofactor activity was predicted based on co-expression modules between factors and candidate target genes and calculated as AUC scores. TF, transcription factor. B: Heatmap showing average regulon activity of hepatocytes for each condition. Representative enriched GO terms related to corresponding regulons are indicated on the right side. C: UMAP visualization showing regulon activity of EZH2 (top) and PPARG (bottom) for indicated conditions. Red circles indicate cycling hepatocyte cluster (upper) and pericentral/midzonal/periportal hepatocyte clusters (bottom). D: GRNs in hepatocytes visualized by Cytoscape. Selected target genes of each regulon are labeled in the network. E: Heatmap showing average regulon activity of HSCs for each condition. Representative enriched GO terms related to the corresponding regulons are indicated on the right side. F: UMAP visualization showing regulon activity of TEAD1 for the indicated conditions. Red circles indicate HSC cluster. G: GRNs in HSCs visualized by Cytoscape. Selected target genes for each regulon are labeled in the network.

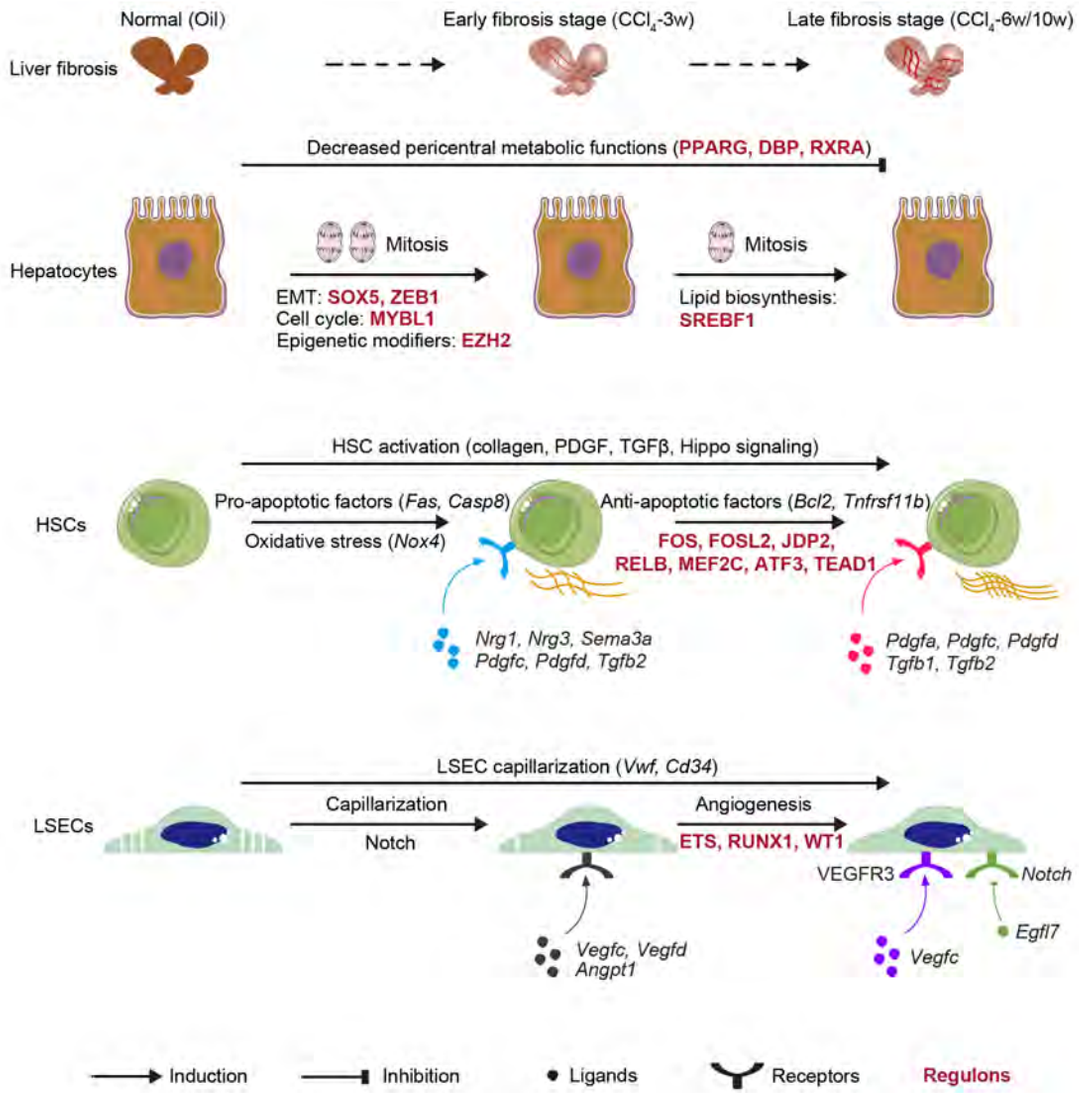

Figure 7 Schematic of stage-specific responses in hepatocytes, HSCs, and LSECs during CCl_4-induced progressive liver fibrosis

counterbalanced during early-stage fibrosis, providing potential therapeutic insights for managing the condition during the later stage.

We also explored intercellular communication dynamics to elucidate how the corresponding networks influence the course of liver fibrosis at different stages. For HSC activation, we revealed that in addition to PDGF and TGFβ signaling, other putative pro-fibrogenic pathways, including neuregulin- and semaphorin 3E-mediated interactions (Yagai et al., 2014), may be involved but only affect early-stage fibrosis, precluding the possibility of targeting these pathways to ameliorate late fibrosis or cirrhosis. This further highlights the importance of clarifying the stage-specific effects of any involved factors to design rational therapies. We also found that pro-angiogenic interactions, including VEGFC-VEGFR3 and ANGPT1-TIE2, were activated in LSECs at the late fibrosis stage. Given that VEGFR2-neutralizing antibody can only partially reverse early fibrosis (Liu et al., 2017) and that VEGFR3 stimulation mediates VEGF-induced angiogenesis, even in the presence of VEGFR2 inhibition (Tammela et al., 2008), it is possible that VEGFR3 may act as an additional relevant regulator of angiogenesis during late-stage fibrosis. Accordingly, the combined suppression of both receptors may have a stronger protective effect than their individual application. In late fibrosis, we also identified increased interactions of *Csf1* with *Csf1r* in Kupffer cells, which promote the accumulation of these cells (Liu et al., 2010; Stutchfield et al., 2015). Previous studies have highlighted that several other immune cell subpopulations, such as monocyte-derived macrophages and NKT cells, modulate both liver fibrosis progression and regression (Tsuchida & Friedman, 2017). Of note, although our dataset is substantial, a larger number of nuclei will be necessary to capture the complete complexity of immune cell responses in CCl_4-induced injury.

We also analyzed the GRNs regulating the progression of liver fibrosis. Based on SCENIC analysis (Aibar et al., 2017) of our dataset, we identified decreased activity in mitosis-related regulons in hepatocytes at the late fibrosis stage, which may help explain the late exhaustion of proliferation capacity. Likewise, we identified a series of known and unknown pro-fibrotic factors with cumulatively increased activity in HSCs and LSECs upon prolonged injury. In addition, we noted that anti-apoptotic NF-κB signaling factor RELB was enriched in L-aHSCs (Kisseleva & Brenner, 2021), further supporting the notion that reactivating pro-apoptotic pathways may be a relevant strategy for reversing late-stage liver fibrosis. In LSECs, apart from the canonical angiogenic ETS family factors, we detected the potential involvement of RUNX1 and

WT1 at the onset of pathological angiogenesis.

In summary, our snRNA-seq atlas of CCl_4 injury provides a rich resource for exploring the molecular dynamics of progressive liver fibrosis and identifying potential clinical targets. Further investigation of our dataset will unveil additional clues and assist in the generation of novel hypotheses. Given the molecular differences between injuries and their effects in different species, it will be important to study whether the events identified here can be recapitulated in other chronic injury models, such as cholestatic injury or non-alcoholic steatohepatitis, and in other species including humans and non-human primates. Lastly, it remains unclear how liver fibrosis progresses spatiotemporally, leaving numerous unanswered questions, such as the full repertoire of scar-associated cell types, spatial vulnerability, and lobule zone-specific responses, which will require further study using high-definition spatially resolved omics technologies (Chen et al., 2022).

DATA AVAILABILITY

All raw data generated in this study have been deposited to the CNGB Nucleotide Sequence Archive under accession code CNP0003569. All processed data can be accessed at Science Data Bank with the link https://doi.org/10.57760/sciencedb.j00139.00049 or Open Archive for Miscellaneous Data in Genome Sequence Archive under accession code OMIX003436.

COMPETING INTERESTS

The authors declare that they have no competing interests.

AUTHORS' CONTRIBUTIONS

P.C.G., M.A.E., and Y.W.L. conceived the idea; M.A.E. and Y.W.L. supervised the work; P.C.G. and Y.W.L. designed the experiments; P.C.G. performed most of the experiments with the help of K.K.H.; P.C.G., J.Z., and Y.W.L. analyzed the data; G.Y.L., X.Z., J.A., J.X.L., L.L., L.W., Y.T.L., D.Y.W., J.S.X., S.J.H., Y.W., R.H.L., W.M., Y.M.S., C.L., and C.Y.L. provided technical support; Z.D., Y.X., A.D.S., M.O., Q.O.Y., F.H., R.F., Y.Y.L., J.L.H., G.V., and L.Q.L. gave relevant advice; M.A.E. and Y.W.L. wrote the manuscript. All authors read and approved the final version of the manuscript.

ACKNOWLEDGEMENTS

We thank all members of our teams, Drs. Da-Hai Zhu and Hu Li (Bioland Laboratory, Guangzhou, China), and the CNGB for their support.

REFERENCES

Adhyatmika A, Beljaars L, Putri KSS, et al. 2020. Osteoprotegerin is more than a possible serum marker in liver fibrosis: a study into its function in human and murine liver. *Pharmaceutics*, **12**(5): 471.

Aibar S, Gonzalez-Blas CB, Moerman T, et al. 2017. SCENIC: single-cell regulatory network inference and clustering. *Nature Methods*, **14**(11): 1083−1086.

Aoyama T, Paik YH, Watanabe S, et al. 2012. Nicotinamide adenine dinucleotide phosphate oxidase in experimental liver fibrosis: GKT137831 as a novel potential therapeutic agent. *Hepatology*, **56**(6): 2316−2327.

Bae WK, Kang K, Yu JH, et al. 2015. The methyltransferases enhancer of zeste homolog (EZH) 1 and EZH2 control hepatocyte homeostasis and regeneration. *The FASEB Journal*, **29**(5): 1653−1662.

Barcena-Varela M, Paish H, Alvarez L, et al. 2021. Epigenetic mechanisms and metabolic reprogramming in fibrogenesis: dual targeting of G9a and DNMT1 for the inhibition of liver fibrosis. *Gut*, **70**(2): 388−400.

Benedito R, Roca C, Sörensen I, et al. 2009. The notch ligands Dll4 and Jagged1 have opposing effects on angiogenesis. *Cell*, **137**(6): 1124−1135.

Ben-Moshe S, Veg T, Manco R, et al. 2022. The spatiotemporal program of zonal liver regeneration following acute injury. *Cell Stem Cell*, **29**(6): 973−989.e10.

Cao Q, Mak KM, Lieber CS. 2002. DLPC decreases TGF-β1-induced collagen mRNA by inhibiting p38 MAPK in hepatic stellate cells. *American Journal of Physiology-Gastrointestinal and Liver Physiology*, **283**(5): G1051−G1061.

Carmeliet P, Jain RK. 2011. Molecular mechanisms and clinical applications of angiogenesis. *Nature*, **473**(7347): 298−307.

Chembazhi UV, Bangru S, Hernaez M, et al. 2021. Cellular plasticity balances the metabolic and proliferation dynamics of a regenerating liver. *Genome Research*, **31**(4): 576−591.

Chen A, Liao S, Cheng MN, et al. 2022. Spatiotemporal transcriptomic atlas of mouse organogenesis using DNA nanoball-patterned arrays. *Cell*, **185**(10): 1777−1792.e21.

Chen F, Jimenez RJ, Sharma K, et al. 2020. Broad distribution of hepatocyte proliferation in liver homeostasis and regeneration. *Cell Stem Cell*, **26**(1): 27−33.e4.

Dai H, Jin QQ, Li L, et al. 2020. Reconstructing gene regulatory networks in single-cell transcriptomic data analysis. *Zoological Research*, **41**(6): 599−604.

Dobie R, Wilson-Kanamori JR, Henderson BEP, et al. 2019. Single-cell transcriptomics uncovers zonation of function in the mesenchyme during liver fibrosis. *Cell Reports*, **29**(7): 1832−1847.e8.

Eraslan G, Drokhlyansky E, Anand S, et al. 2022. Single-nucleus cross-tissue molecular reference maps toward understanding disease gene function. *Science*, **376**(6594): eabl4290.

Filliol A, Saito Y, Nair A, et al. 2022. Opposing roles of hepatic stellate cell subpopulations in hepatocarcinogenesis. *Nature*, **610**(7931): 356−365.

Gachon F, Olela FF, Schaad O, et al. 2006. The circadian PAR-domain basic leucine zipper transcription factors DBP, TEF, and HLF modulate basal and inducible xenobiotic detoxification. *Cell Metabolism*, **4**(1): 25−36.

Gonzalez SA, Fiel MI, Sauk J, et al. 2009. Inverse association between hepatic stellate cell apoptosis and fibrosis in chronic hepatitis C virus infection. *Journal of Viral Hepatitis*, **16**(2): 141−148.

Halpern KB, Shenhav R, Matcovitch-Natan O, et al. 2017. Single-cell spatial reconstruction reveals global division of labour in the mammalian liver. *Nature*, **542**(7641): 352−356.

Han L, Wei XY, Liu CY, et al. 2022. Cell transcriptomic atlas of the non-human primate *Macaca fascicularis*. *Nature*, **604**(7907): 723–731.

Jin SQ, Guerrero-Juarez CF, Zhang LH, et al. 2021. Inference and analysis of cell-cell communication using CellChat. *Nature Communications*, **12**(1): 1088.

Kim YO, Popov Y, Schuppan D. 2017. Optimized mouse models for liver fibrosis. *In*: Clausen BE, Laman JD. Inflammation: Methods and Protocols. New York: Humana Press, 279–296.

Kisseleva T, Brenner D. 2021. Molecular and cellular mechanisms of liver fibrosis and its regression. *Nature Reviews Gastroenterology & Hepatology*, **18**(3): 151−166.

Korsunsky I, Millard N, Fan J, et al. 2019. Fast, sensitive and accurate integration of single-cell data with Harmony. *Nature Methods*, **16**(12): 1289−1296.

Kostallari E, Wei B, Sicard D, et al. 2022. Stiffness is associated with hepatic stellate cell heterogeneity during liver fibrosis. *American Journal of Physiology-Gastrointestinal and Liver Physiology*, **322**(2): G234−G246.

Krenkel O, Hundertmark J, Ritz TP, et al. 2019. Single cell RNA sequencing identifies subsets of hepatic stellate cells and myofibroblasts in liver fibrosis. *Cells*, **8**(5): 503.

Lafoz E, Ruart M, Anton A, et al. 2020. The endothelium as a driver of liver fibrosis and regeneration. *Cells*, **9**(4): 929.

Lam JD, Oh DJ, Wong LL, et al. 2017. Identification of RUNX1 as a mediator of aberrant retinal angiogenesis. *Diabetes*, **66**(7): 1950−1956.

Lan T, Kisseleva T, Brenner DA. 2015. Deficiency of NOX1 or NOX4 prevents liver inflammation and fibrosis in mice through inhibition of hepatic stellate cell activation. *PLoS One*, **10**(7): e0129743.

Lee YS, Jeong WI. 2012. Retinoic acids and hepatic stellate cells in liver disease. *Journal of Gastroenterology and Hepatology*, **27**(Suppl 2): 75−79.

Lin Y, Chen NT, Shih YP, et al. 2010. DLC2 modulates angiogenic responses in vascular endothelial cells by regulating cell attachment and migration. *Oncogene*, **29**(20): 3010−3016.

Liu C, Tao Q, Sun MY, et al. 2010. Kupffer cells are associated with apoptosis, inflammation and fibrotic effects in hepatic fibrosis in rats. *Laboratory Investigation*, **90**(12): 1805−1816.

Liu LW, You ZF, Yu HS, et al. 2017. Mechanotransduction-modulated fibrotic microniches reveal the contribution of angiogenesis in liver fibrosis. *Nature Materials*, **16**(12): 1252−1261.

Ma Q, Ma WJ, Song TZ, et al. 2022. Single-nucleus transcriptomic profiling of multiple organs in a rhesus macaque model of SARS-CoV-2 infection. *Zoological Research*, **43**(6): 1041−1062.

Macchi F, Sadler KC. 2020. Unraveling the epigenetic basis of liver development, regeneration and disease. *Trends in Genetics*, **36**(8): 587−597.

Macnair W, Gupta R, Claassen M. 2022. Psupertime: supervised pseudotime analysis for time-series single-cell RNA-seq data. *Bioinformatics*, **38**(S1): i290−i298.

Mannaerts I, Leite SB, Verhulst S, et al. 2015. The Hippo pathway effector YAP controls mouse hepatic stellate cell activation. *Journal of Hepatology*, **63**(3): 679−688.

Mederacke I, Filliol A, Affo S, et al. 2022. The purinergic P2Y14 receptor links hepatocyte death to hepatic stellate cell activation and fibrogenesis in the liver. *Science Translational Medicine*, **14**(639): eabe5795.

Michalopoulos GK, Bhushan B. 2021. Liver regeneration: biological and pathological mechanisms and implications. *Nature Reviews Gastroenterology & Hepatology*, **18**(1): 40−55.

Mühleder S, Fernández-Chacón M, Garcia-Gonzalez I, et al. 2021. Endothelial sprouting, proliferation, or senescence: tipping the balance from physiology to pathology. *Cellular and Molecular Life Sciences*, **78**(4): 1329−1354.

Oettgen P. 2010. The role of ets factors in tumor angiogenesis. *Journal of Oncology*, **2010**: 767384.

Ogaly HA, Eltablawy NA, El-Behairy AM, et al. 2015. Hepatocyte growth factor mediates the antifibrogenic action of *Ocimum bacilicum* essential oil against CCl_4-Induced liver fibrosis in rats. *Molecules*, **20**(8): 13518−13535.

Poisson J, Lemoinne S, Boulanger C, et al. 2017. Liver sinusoidal endothelial cells: physiology and role in liver diseases. *Journal of Hepatology*, **66**(1): 212−227.

Qiu XJ, Hill A, Packer J, et al. 2017. Single-cell mRNA quantification and differential analysis with Census. *Nature Methods*, **14**(3): 309−315.

Ramachandran P, Dobie R, Wilson-Kanamori JR, et al. 2019. Resolving the fibrotic niche of human liver cirrhosis at single-cell level. *Nature*, **575**(7783): 512−518.

Roehlen N, Crouchet E, Baumert TF. 2020. Liver fibrosis: mechanistic concepts and therapeutic perspectives. *Cells*, **9**(4): 875.

Sarin SK, Kumar M, Eslam M, et al. 2020. Liver diseases in the asia-pacific region: a *Lancet gastroenterology* & *Hepatology* commission. *Lancet Gastroenterol Hepatol*, **5**(2): 167−228.

Schmidt MHH, Bicker F, Nikolic I, et al. 2009. Epidermal growth factor-like domain 7 (EGFL7) modulates Notch signalling and affects neural stem cell renewal. *Nature Cell Biology*, **11**(7): 873−880.

Sebastiano V, Dalvai M, Gentile L, et al. 2010. Oct1 regulates trophoblast development during early mouse embryogenesis. *Development*, **137**(21): 3551−3560.

Shiojiri N, Kametani H, Ota N, et al. 2018. Phylogenetic analyses of the hepatic architecture in vertebrates. *Journal of Anatomy*, **232**(2): 200−213.

Slyper M, Porter CBM, Ashenberg O, et al. 2020. A single-cell and single-nucleus RNA-Seq toolbox for fresh and frozen human tumors. *Nature Medicine*, **26**(5): 792−802.

Stutchfield BM, Antoine DJ, Mackinnon AC, et al. 2015. CSF1 restores innate immunity after liver injury in mice and serum levels indicate outcomes of patients with acute liver failure. *Gastroenterology*, **149**(7): 1896−1909.e14.

Su TT, Yang YL, Lai SC, et al. 2021. Single-cell transcriptomics reveals zone-specific alterations of liver sinusoidal endothelial cells in cirrhosis. *Cellular and Molecular Gastroenterology and Hepatology*, **11**(4): 1139−1161.

Tahara Y, Shibata S. 2016. Circadian rhythms of liver physiology and disease: experimental and clinical evidence. *Nature Reviews Gastroenterology & Hepatology*, **13**(4): 217−226.

Tammela T, Zarkada G, Wallgard E, et al. 2008. Blocking VEGFR-3 suppresses angiogenic sprouting and vascular network formation. *Nature*, **454**(7204): 656−660.

Terkelsen MK, Bendixen SM, Hansen D, et al. 2020. Transcriptional dynamics of hepatic sinusoid-associated cells after liver injury. *Hepatology*, **72**(6): 2119−2133.

Tsuchida T, Friedman SL. 2017. Mechanisms of hepatic stellate cell activation. *Nature Reviews Gastroenterology & Hepatology*, **14**(7): 397−411.

Wagner A, Regev A, Yosef N. 2016. Revealing the vectors of cellular identity with single-cell genomics. *Nature Biotechnology*, **34**(11): 1145−1160.

Wagner KD, Cherfils-Vicini J, Hosen N, et al. 2014. The Wilms' tumour suppressor Wt1 is a major regulator of tumour angiogenesis and progression. *Nature Communications*, **5**: 5852.

Wang D, Han S, Wang X, et al. 2015. SOX5 promotes epithelial-mesenchymal transition and cell invasion via regulation of Twist1 in hepatocellular carcinoma. *Medical Oncology*, **32**(2): 461.

Wang S, Zhang C, Hasson D, et al. 2019. Epigenetic compensation promotes liver regeneration. *Developmental Cell*, **50**(1): 43−56.e6.

Wolf FA, Angerer P, Theis FJ. 2018. SCANPY: large-scale single-cell gene expression data analysis. *Genome Biology*, **19**(1): 15.

Xu SS, Li Y, Wang HP, et al. 2023. Depletion of *stearoyl-CoA desaturase* (*scd*) leads to fatty liver disease and defective mating behavior in zebrafish. *Zoological Research*, **44**(1): 63−77.

Yagai T, Miyajima A, Tanaka M. 2014. Semaphorin 3E secreted by damaged hepatocytes regulates the sinusoidal regeneration and liver fibrosis during liver regeneration. *The American Journal of Pathology*, **184**(8): 2250−2259.

Yang W, He H, Wang TT, et al. 2021. Single-cell transcriptomic analysis reveals a hepatic stellate cell-activation roadmap and myofibroblast origin during liver fibrosis in mice. *Hepatology*, **74**(5): 2774−2790.

Young MD, Behjati S. 2020. SoupX removes ambient RNA contamination from droplet-based single-cell RNA sequencing data. *Gigascience*, **9**(12): giaa151.

Zaret KS. 2002. Regulatory phases of early liver development: paradigms of organogenesis. *Nature Reviews Genetics*, **3**(7): 499−512.

Zhang WW, Ping J, Zhou Y, et al. 2019. Salvianolic acid b inhibits activation of human primary hepatic stellate cells through downregulation of the myocyte enhancer factor 2 signaling pathway. *Frontiers in Pharmacology*, **10**: 322.

Zhang X, Lai GY, Volpe G, et al. 2022. Towards a primate single-cell atlas. *Zoological Research*, **43**(4): 691−694.

Zhou YY, Zhou B, Pache L, et al. 2019. Metascape provides a biologist-oriented resource for the analysis of systems-level datasets. *Nature Communications*, **10**(1): 1523.